Article

Near Field Sensing Applications with Tunable Beam Millimeter Wave Antenna Sensors in an All-in-One Chip Design

Ming-An Chung * , **Chia-Wei Lin and Wei-Jen Lo**

Department of Electronic Engineering, National Taipei University of Technology, Taipei 10608, Taiwan;
t109369011@ntut.edu.tw (C.-W.L.); t109368119@ntut.edu.tw (W.-J.L.)
* Correspondence: minganchung@ntut.edu.tw

Abstract: In this paper, a single-band beam control antenna is designed with a parallel coupler to realize a microstrip patch antenna passive wireless sensor in the form of a chip. It has a phase shift characteristic of the antenna radiation direction in the positive and negative directions. The antenna includes an orthogonal direction coupler design with a 90° parallel coupler in phase using a special structure that allows the whole chip area to be miniaturized while allowing the main beam angle to have a directivity function. The coupler is designed for the 28 GHz millimeter wave band. After feeding the patch antenna at the output port of the coupler and simultaneously feeding the excitation at the input port, the beam phase changes to +45° and +135° with a phase difference of 90°. The designed antenna size is 1160 μm × 790 μm, and the overall IC size is 1.2 mm × 1.2 mm. The power density simulation shows that the maximum power density is only 0.00797 W/kg for a 1 cm^2 human sampling area, which means that the antenna sensor is suitable for use on human surfaces.

Keywords: antenna sensor; wearable sensor; parallel coupler; chip antenna; millimeter wave

1. Introduction

With the advancement of the chip manufacturing process, the miniaturization of components has advanced to a whole new level. The antenna and millimeter wave circuits can be easily integrated into a single chip. Compared to wired sensor devices, wireless sensors have more advantages because they do not require wires to provide a transmission path, so they are easy to install and less expensive to maintain. The wireless transmission sensor can skip the setup of the sensor network, as well as expand the maximum physical limitations of the connection to the sensor. Wireless sensors are differentiated into active and passive wireless sensors. Applications of passive wireless sensors include passive radar [1–5], liquid sensing [6–8], spatial positioning [9–13], RFID [14–21], and blood glucose determination [22,23].

Passive wireless sensors are a core technology in many fields, such as the Internet of Things [24,25], smart cities [26], and smart healthcare [22,23,27]. Many designs in wireless sensing systems utilize a branch coupler for both outputs, which can be used to ensure that the strength of the two signals is equal [20,28,29]. With the evolution of a large number of sensors, a complex environment full of signal scattering interference has been created.

Many researchers are currently proposing microstrip patch antenna passive wireless sensors for studies such as detecting cracks on the surface of an object [30–32]. The resonant frequency can be clearly known under a stationary ground plane. Assuming a discontinuity in the ground plane, the resonant frequency is varied to detect cracks on the ground plane. Otherwise, the physical properties of the material can be measured by beam control. For example, in [33], the microwave frequency band was used to detect foreign material in uncleaned peanuts without shells by using the good detection effect of watery items. Compared to X-ray and infrared instruments, it has the advantage of being more cost effective. The common patch antenna is composed of two layers of metal and dielectric

substrate [34], and the resonant frequency of the antenna is changed by adjusting the geometric length and width of the upper metal surface [35,36].

Beam control is the change of the main flap beam to the desired beam angle. For example, a parallel coupler makes a Beam Forming Network (BFN) designed to individually distribute the feed and phase at some degree of variation at the feed port. Alternatively, LC circuits [37], phase shifters [38,39], and phase shifters with diodes can be used to achieve beam angle switching [40–43]. The main beam can be mechanically steered using hardware devices such as motors or drivers with control software [44] to steer the radiation field pattern emitted by the guided antenna.

There are many studies investigating millimeter-wave microstrip patch antenna passive wireless sensors [45,46]. Non-contact measurement systems are suitable for liquid measurements, while millimeter wave sensors without power supply have the advantage of being maintenance-free and have a very long service life. Non-contact millimeter wave sensors are highly flexible, can measure in harsh environments, and are not easily destroyed. The signal can be easily transmitted through the fog and dust, not affected by the changing light conditions [47], and the accuracy is similar to that of laser sensors. It can also measure at high repetition rates and simultaneously measure the speed of the target at a low cost. Millimeter wave sensors that do not require power are also suitable for imaging applications, including contraband detection for flight safety and indoor space imaging because the wavelengths of radiation are long enough that they propagate through clothing, furniture, and other coverings and short enough to provide a high resolution [48].

Contact measurement systems are often used in wearable antenna sensors. Wearable antenna sensors come into contact with the human body, and the antenna is susceptible to the high dielectric constant of the human body, which changes the resonant frequency, gain, and efficiency. On the other hand, antennas can cause radiated effects on the human body. To solve both problems, researchers have changed the antenna substrate materials to allow these wearable antenna sensors to achieve better antenna gain, efficiency, lower human absorption ratio, and lower power density through material improvements and changes in antenna shape designs, such as electromagnetic band gap (EBG), artificial magnetic conductor (AMC) [49], and high impedance surface (HIS) [50].

In this paper, a microstrip patch antenna passive wireless sensor is developed on a chip. By improving the design, the coupler and the patch antenna size are successfully miniaturized. In this design, a parallel coupler is used to complete the beam control and achieve 90° phase switching. With the variation of the patch antenna, such as rectangular gap, symmetrical metal ring and PSL technology, the performance is improved and the cost is significantly reduced without increasing the usage area. In order to make the antenna sensor developed in this paper applicable to the human body surface, power density (PD) simulation is added. The simulation results are also fully compliant with FCC, ICNIRP, and IEEE specifications for PD values, which means that the designed chip is quite suitable for use in wearable devices. Compared to the branch and ring couplers, the parallel couplers can operate at any power distribution and provide a 90° phase difference [37,39]. It also allows the beam to produce a 90-degree scanning range and detects the size of the actual object by using the change of the beam close to the object, thus achieving the object scanning function. This study is to simulate the antenna characteristics using ANSYS HFSS.

2. Related Work

2.1. Subsection

Figure 1 shows the schematic diagram of the parallel coupler. Figure 2 shows the equivalent model of the parallel coupler, which contains a pair of mutual inductors, self-inductors L_s and mutual inductance coupling coefficient k. Capacitance C_m and C_p denote the parasitic capacitance between ground and winding. The ideal parallel coupler design is for port two and port four, where port two is in phase at 0 degrees and port four is in phase at 90 degrees, and the two ports have equal phase differences of 90° in magnitude. The polarization generated by input port one or port three will achieve excellent linear

polarization (LP) operation when the patch is perfectly matched at port two and port four. In addition, the ideal parallel coupler that couples to port three has very little power effect, thus producing a high level of isolation. The biggest limitation of this conventional configuration is that parallel couplers usually have only a narrow frequency band. Another technical disadvantage is that parallel couplers usually take up a large amount of space, resulting in an increase in overall size.
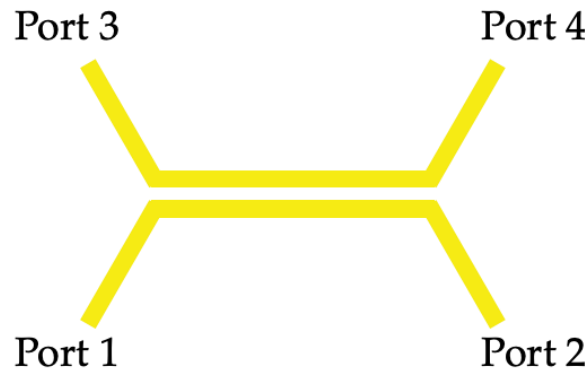

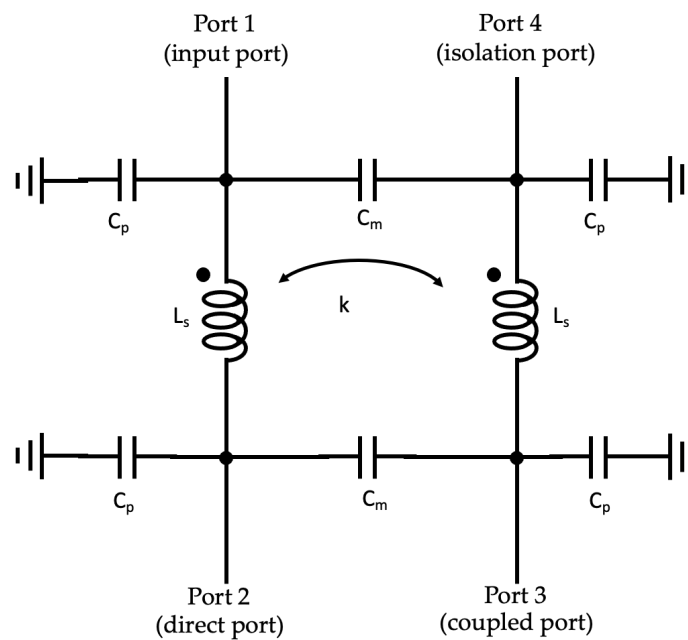**Figure 1.** Traditional parallel coupler shape.

Figure 2. The equivalent circuit model of the parallel coupler; C_m and C_p are the parasitic capacitances between the two parallel lines and the parallel line to ground, respectively.

2.2. Microstrip Line Antenna Structure

A schematic diagram of a microstrip line chip antenna is shown in Figure 3. The mathematical equations for the length and width of a microstrip patch antenna are [51,52]:

$$W_p = \frac{c}{2f_r}\sqrt{\frac{2}{\varepsilon_r + 1}} \tag{1}$$

$$\Delta L_p = 0.712t\frac{(\varepsilon_{eff} + 0.3)\left[\frac{w_p}{t} + 0.264\right]}{(\varepsilon_{eff} - 0.258)\left[\frac{w_p}{t} + 0.813\right]} \tag{2}$$

$$L_p = \frac{c}{2f_r\sqrt{\varepsilon_{eff}}} - 2\Delta L_p \tag{3}$$

where w_p is the width of the patch antenna, L_p is the length of the patch antenna, and t is the thickness of the substrate, as shown in Figure 3. ΔL_p is used to describe the effect on the edge effect when the length of the antenna is adjusted such that the edge effect is decreased when the length of the antenna is reduced. ε_r is the permittivity. c is the wave speed in free space. ε_{eff} is the equivalent permittivity.

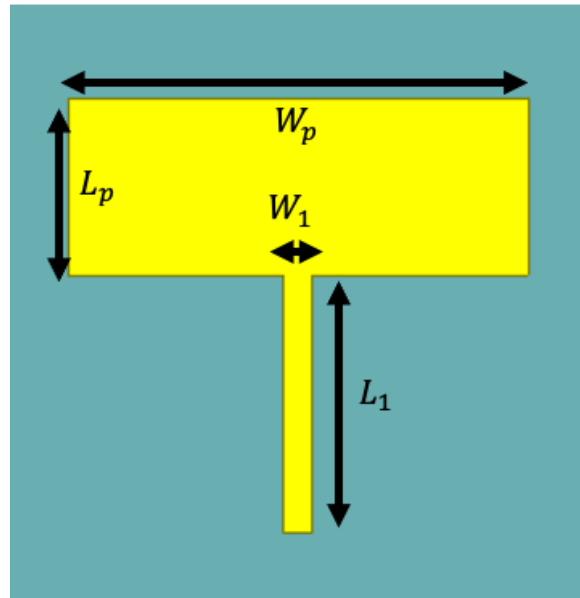**Figure 3.** Conventional microstrip line chip antenna structure (The parameters are: $L_p = 150$ μm, $W_p = 90$ μm, $L_1 = 210$ μm, and $W_1 = 25$ μm).

Take the traditional PCB antenna design for example, the antenna body is designed on the surface metal layer. From the resistivity laws [53]:

$$R = \rho \frac{\iota}{A} \tag{4}$$

R is the resistance, ρ is the resistivity, ι is the length, and A is the cross-sectional area. When the cross-sectional area of each unit is larger, the resistance value will be smaller, and the transmission loss will also be smaller. In the design of the patch antenna, this characteristic is used to design the antenna with the main beam direction facing upward and then make the reflective surface through the back metal to enhance the antenna gain [54].

3. Chip Layout and Design

As the frequency increases, the transmission loss between the antenna and the RF circuit becomes very high. In this study, the finished product is designed for 28 GHz, which is one of the millimeter wave bands used in most countries today. The chip antenna is very helpful in reducing the transmission loss by significantly shortening the connection distance between the RF circuit and the antenna.

3.1. Parallel Coupler Design

The common coupler types are Parallel-line coupler, Branch-line coupler [55–59], Rat-race coupler [56,57,60–62], Lange coupler, Directional coupler [63–65], Lumped-Element coupler [66], and Hybrid coupler [67,68]. The design can be achieved by various structures such as Coplanar waveguide (CPW), Substrate-integrated waveguide (SIW), Microstrip line, etc. In this design, the parallel coupler structure is chosen and designed in the form of a microstrip line.

Quadrature couplers are usually designed as parallel line couplers or branch couplers [69], both of which are designed based on a quarter wavelength transmission line. However, this design is still too large for a frequency of 28 GHz.

By calculating the wavelength g through Equation (5), we can obtain the $1/4\lambda$ length at 28 GHz, which is equal to about 1.33 mm. Equation (6) is to calculate the equivalent dielectric constant ε_{eff}, ε_r is the dielectric constant, H is the substrate thickness, W is the microstrip line width, and T is the aluminum thickness [52].

$$\lambda_g = \frac{300}{f_{GHz}\sqrt{\varepsilon_{eff}}} \tag{5}$$

$$\varepsilon_{eff} = \frac{\varepsilon_r + 1}{2} + \frac{\varepsilon_r - 1}{2} \left\{ \frac{1}{\sqrt{1 + 12\left(\frac{H}{W}\right)}} + 0.04\left[1 - \left(\frac{W}{H}\right)^2\right] \right\} \tag{6}$$

The standard CMOS implementation of a parallel coupler is achieved using a CMOS multi-metal layer structure with a wide-sided coupling. Figure 4 shows an example layout where the parallel coupler is placed between the top and second layers to increase the coupling amount by direct stacking. The first winding layout starting from port 1 is on the thinner metal 6 layer with a thickness of 2.34 μm and then along the metal 6 layer to port 2. Meanwhile, the second winding is placed on the metal 5 layer starting from port 3 with a thickness of 0.53 μm and then completely overlaps with the metal 6 winding. The grounding layer below the stacked windings is removed to obtain a high k value. By this improvement in architecture, about 50% of the usable area can be saved [69].
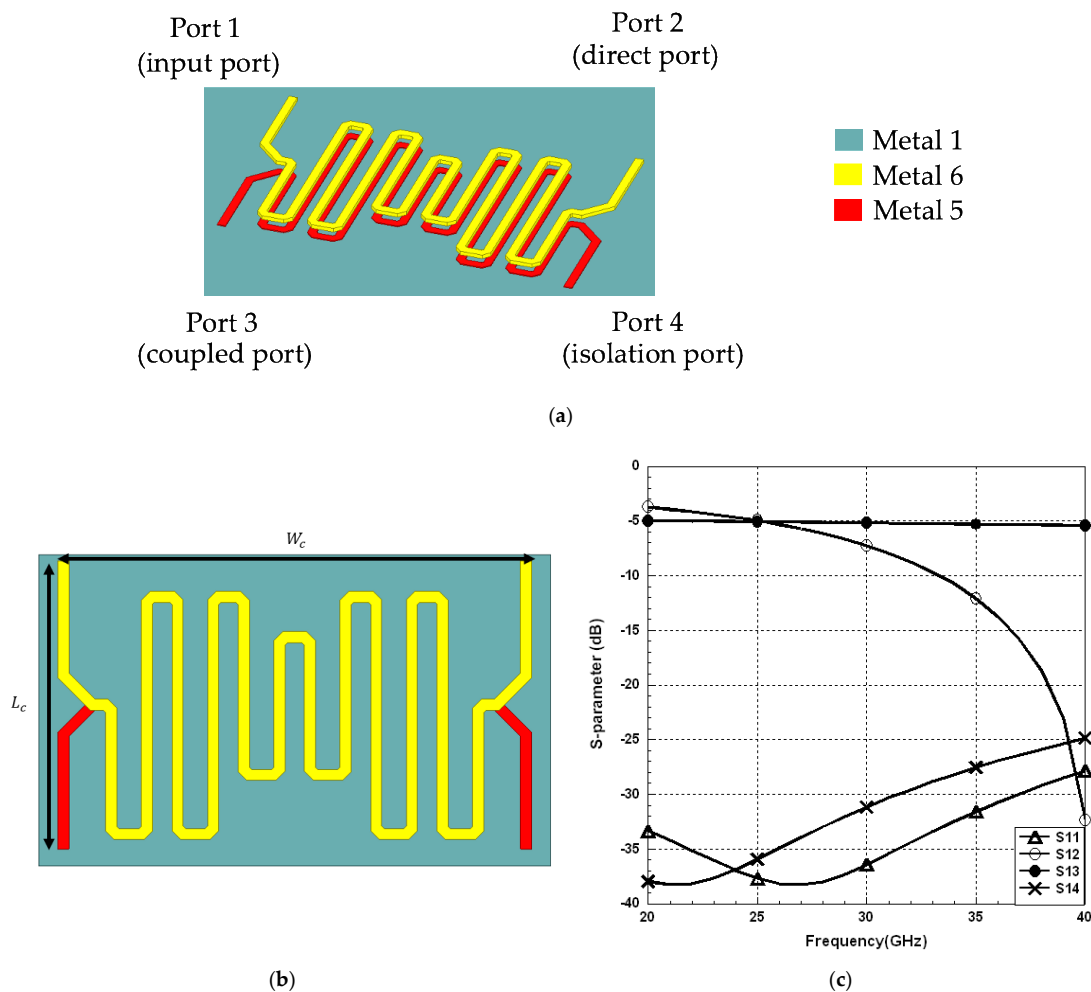

(a)

(b)

(c)

Figure 4. (**a**)The layout of the proposed design of the parallel coupler. (**b**) View from the top, $L_C = 0.216$ μm, and $W_c = 0.129$ μm. (**c**) S-parameters include S_{11}, S_{12}, S_{13}, and S_{14} for coupler.

3.2. Structure of Microstrip Line Chip Antenna

3.2.1. Antenna Stacking Design

As shown in Figure 4, the parallel coupler designed in this paper has four ports, so two sets of antennas of Figure 3 are needed to form a symmetrical antenna structure as in Figure 5. The antenna dimensions are $L_P = 150$ µm, $W_P = 90$ µm, $L_1 = 210$ µm, and $W_1 = 25$ µm. In order to improve the antenna gain, two antenna structures of Figure 5 are formed as Figure 6, where $L_2 = 210$ µm and $W_2 = 164.5$ µm. Figure 7 shows the simulated antenna gain for both Figures 5 and 6 in antenna structures. The diamond-shaped curve "antenna" in Figure 7 is the antenna gain of Figure 5. The "x" curve in Figure 7, "Series antenna", is the antenna gain for Figure 6. So, Figure 7 clearly shows that the antenna structure of Figure 6 is indeed able to increase the gain.
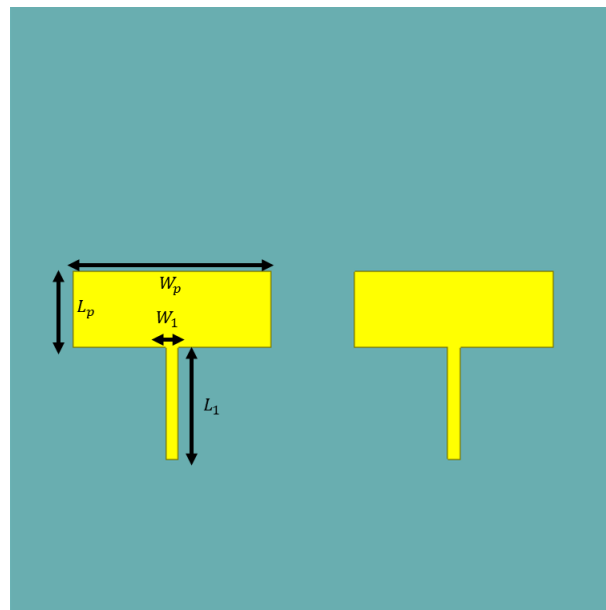

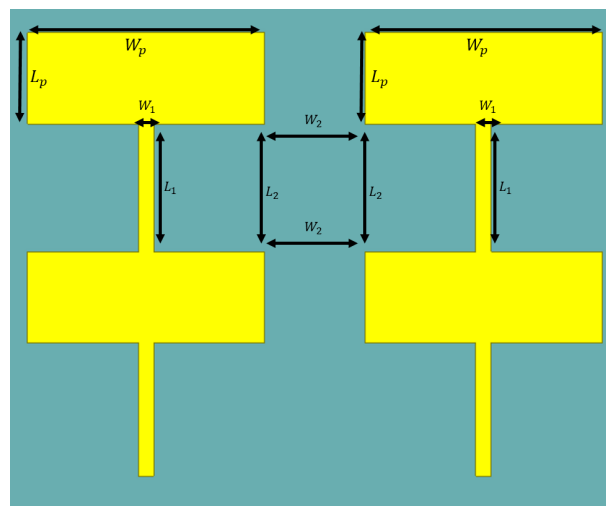**Figure 5.** The initial design of the proposed chip antenna.

Figure 6. A structure in which two sets of initially designed antennas are stacked together.
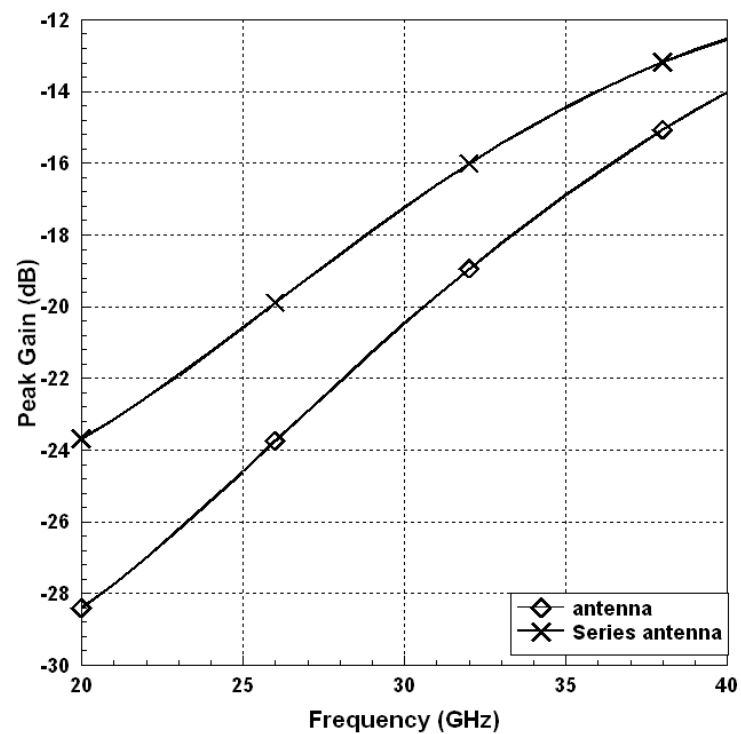
Figure 7. Comparison of the gain of the chip antenna stacked structure with the unstacked one.

3.2.2. Rectangular Slot

To improve the performance of the chip, a chip antenna with a rectangular slot is proposed in this study, as shown in Figure 8. As shown in Figure 9, the available bandwidth is narrower without the rectangular slot, and the standard $S_{11} < -10$ dB can produce a bandwidth of 12–60 GHz.
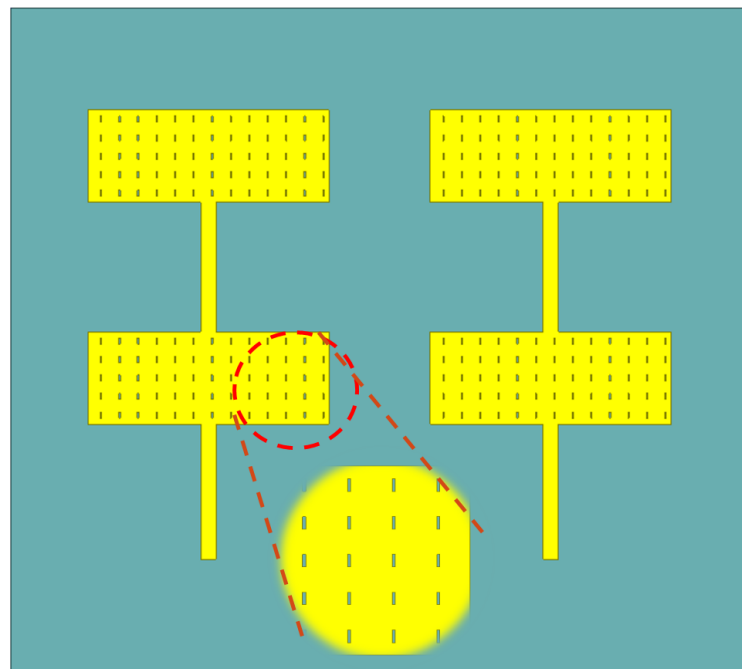

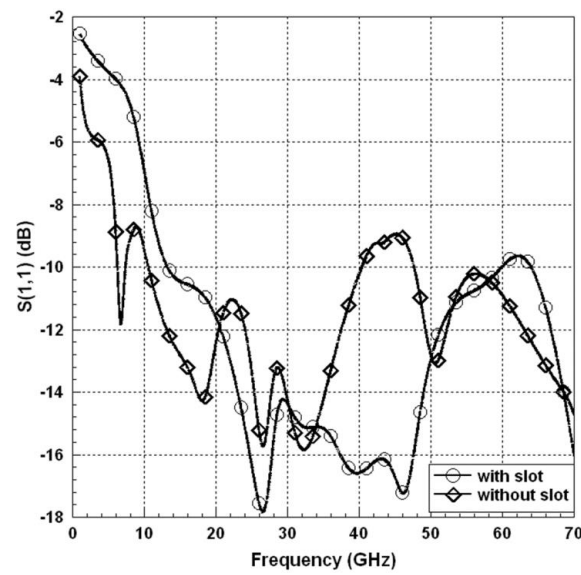**Figure 8.** Add a rectangular slot to the antenna body.

Figure 9. Comparison of S-parameters with and without rectangular slot.

3.2.3. Gain Enhancement

In [70], asymmetric square metal rings are described for achieving Gain Enhancement to improve the overall gain. By using this concept, the square metal ring design is added to the antenna of Figure 8 and makes it symmetrical, as shown in Figure 10. Figures 11 and 12 show the simulated field pattern without and with the addition of symmetric square metal rings, respectively. Figure 11a–c shows the *x-y*, *x-z*, and *y-z* planar field patterns when port 1 is fed in, and Figure 11d–f shows the *x-y*, *x-z*, and *y-z* planar field pattern when port 3 is fed in. Figure 12a–c shows the *x-y*, *x-z*, and *y-z* planar field pattern when port 1 is fed in, and Figure 12d–f shows the *x-y*, *x-z*, and *y-z* planar fields when port 3 is fed in. Comparing Figures 11 and 12, the beam can be guided to the correct direction when a symmetric square metal ring is added.
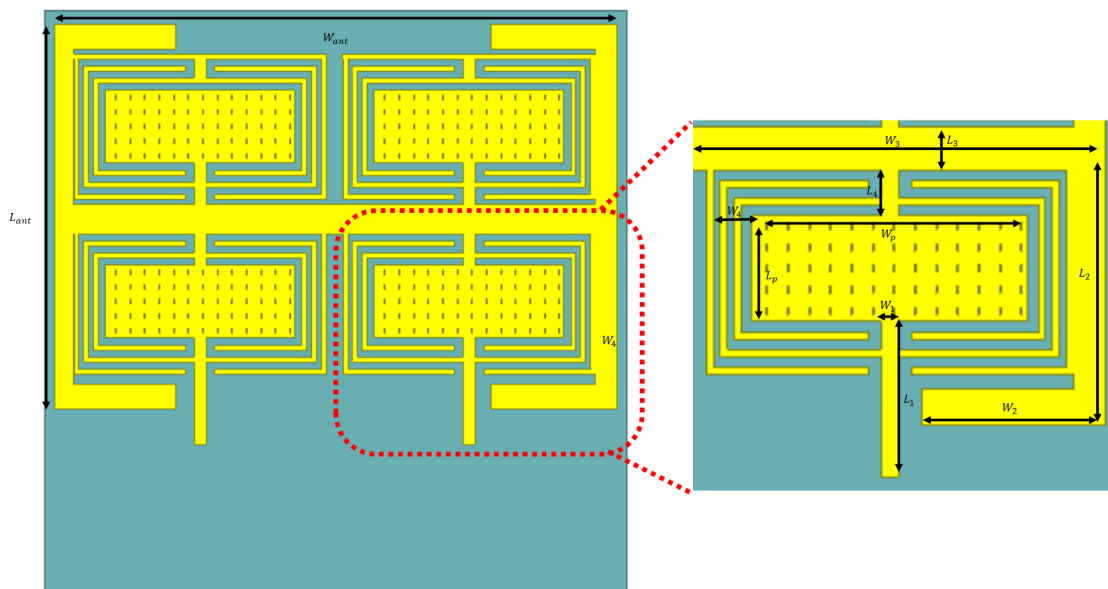

Figure 10. Antenna body with symmetrical square metal ring (The parameters are: $L_{ant} = 760$ μm, $W_{ant} = 1145$ μm, $W_1 = 25$ μm, $W_2 = 250$ μm, $W_3 = 575$ μm, $W_4 = 55$ μm, $L_1 = 210$ μm, $L_2 = 345$ μm, $L_3 = 60$ μm, $L_4 = 64.5$ μm, and metal ring fine wire diameter = 10 μm).
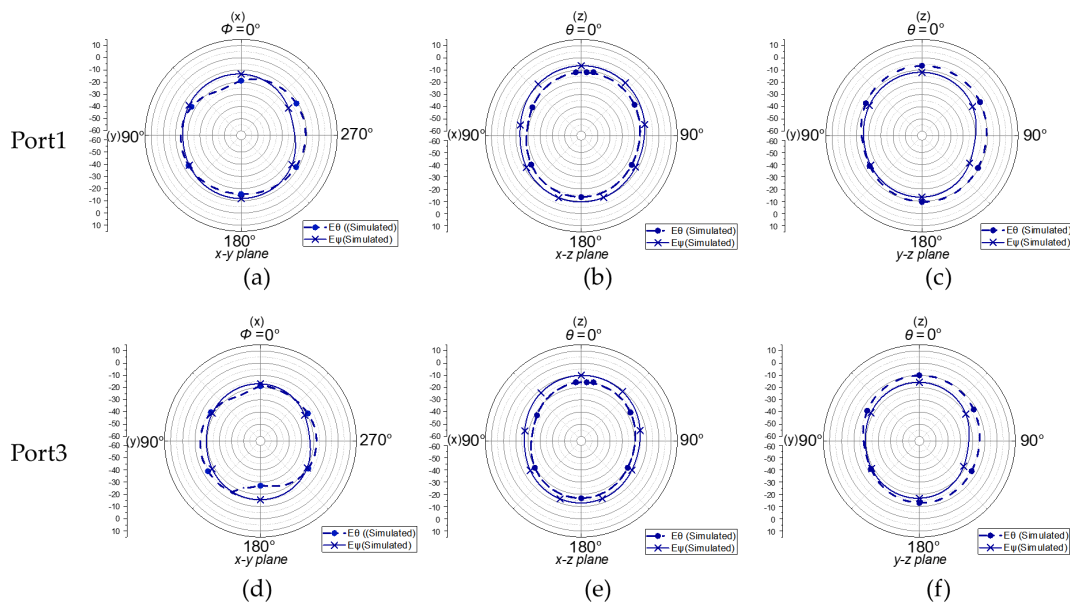
Figure 11. The *x-y*, *x-z*, and *y-z* planar field patterns without the metal ring are (**a**–**c**) for port 1 feed and (**d**–**f**) for port 3 feed.
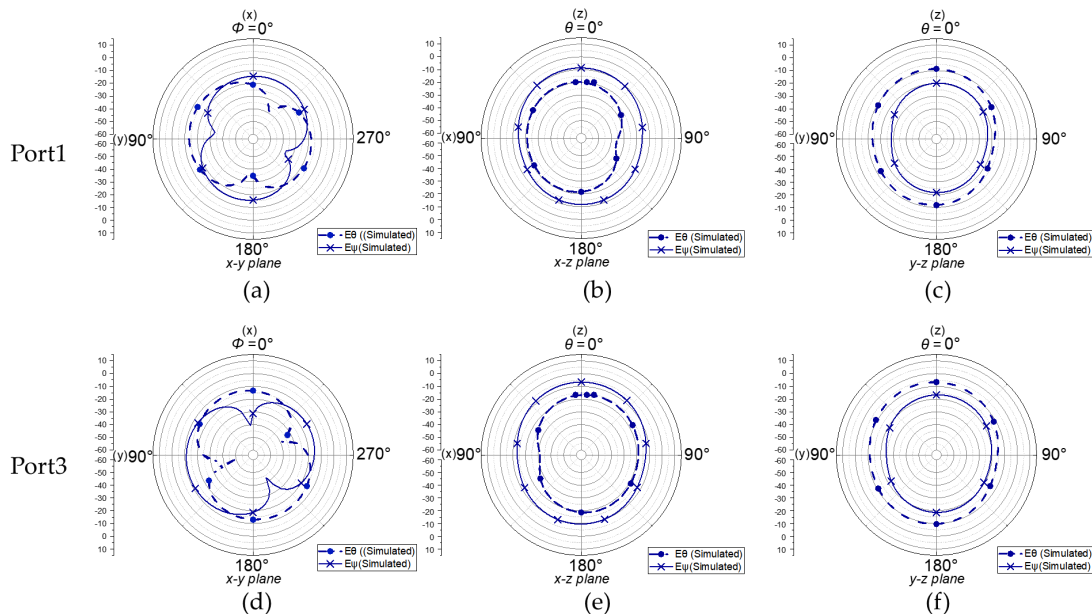
Figure 12. Adding the *x-y*, *x-z*, and *y-z* plane field patterns of the metal ring, (**a**–**c**) for port 1 feed and (**d**–**f**) for port 3 feed.

3.2.4. Partially Shield Layer

In order to further enhance the antenna gain, the PSL (partially shield layer) technique is added [71], as in Figure 13. Metal PSL is first added to metal layer 2, and then the bottom metal layer, metal 1, is hollowed out in a symmetrical manner for the defective ground structure (DGS), as in Figure 14. An additional capacitive element is created between the top metal and PSL layers to effectively converge the resonant frequencies, resulting in a smaller antenna size and improved gain. As shown in Figure 15, a bandwidth of 12~60 GHz can be generated at $S_{11} < -10$ dB.
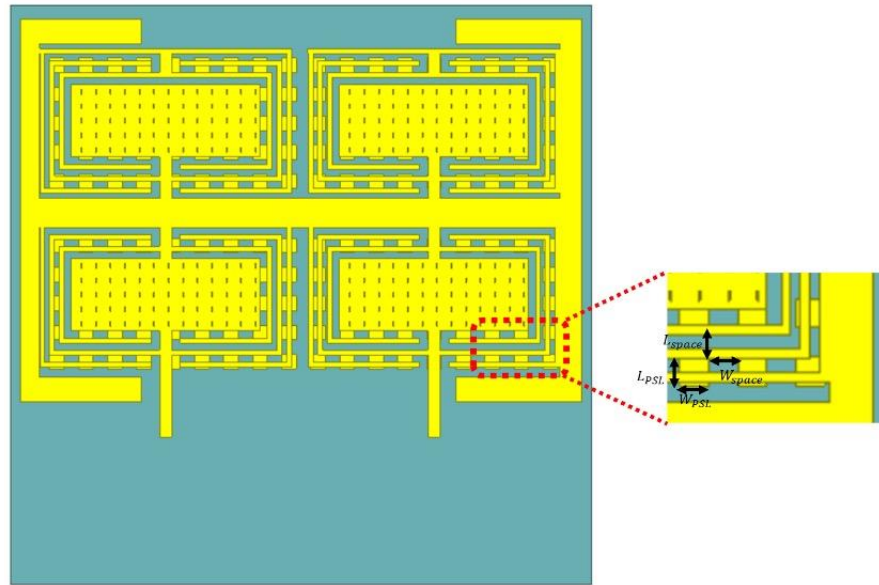
Figure 13. Antenna body plus symmetrical square metal ring and PSL (The parameters are: $L_{PSL} = 30$ μm, $W_{PSL} = 30$ μm, $L_{space} = 30$ μm, and $W_{space} = 30$ μm).
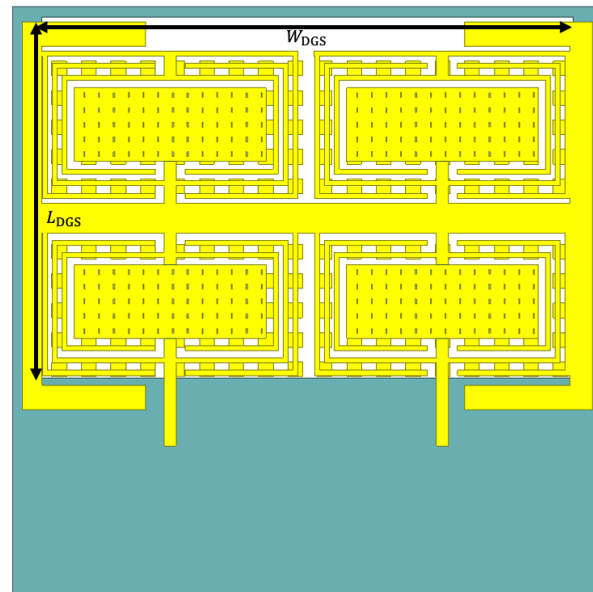
Figure 14. Add DGS and hollow out the metal at the bottom (The parameters are: $L_{DGS} = 735$ μm, and $W_{DGS} = 1080$ μm).

From Equation (7), the parallel plate capacitor formed by two metal layers filled with oxide has a larger capacitance, allowing the center frequency of the antenna to be effectively reduced. As the thickness of the oxide increases, the effective capacitance decreases, the frequency shifts to higher frequencies again, and the input reflection impedance is better [71].

$$f_r \propto \frac{1}{\sqrt{C_{eq}}} \tag{7}$$

where f_r is the resonant frequency. C_{eq} is the value of the capacitance between the metal layers, that is, the equivalent capacitance between the top metal and the PSL.
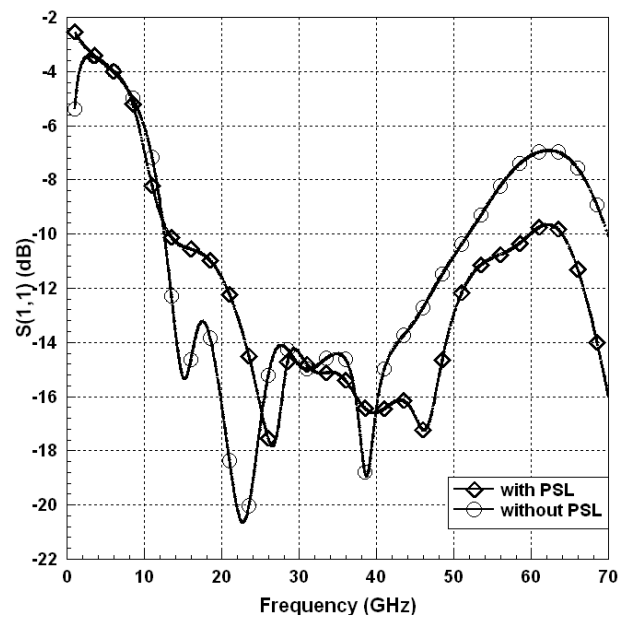
Figure 15. Comparison of PSL with and without PSL.

3.3. Proposed IC Design

In this paper, we propose a solution as shown in Figure 16, combining the structure of Figures 4 and 14. In this particular design, the antenna is patterned on a 600-micron-thick silicon substrate using 2.34-micron aluminum as the conductor. The designed antenna size is 1160 μm × 790 μm. One of the keys to successfully designing a chip on a silicon semiconductor chip is to comply with metal density design rules. Even at millimeter wave frequencies, the antenna can be small enough to fit on the chip, but it is still the largest component on the chip. Figure 17a shows the proposed antenna in the TSMC 0.18 μm CMOS process using the metal layers, which shows that the lowest layer of the substrate is made of silicon, and metals 1–6 are made of aluminum. The layers used in this design are metal 1, metal 2, metal 5, and metal 6. The thicknesses of each layer are 0.53 μm for metal 1 and 5 and 2.34 μm for metal 6. The antenna and coupler are designed using metal 6.

Figure 16. Geometry of the proposed linearly polarized antenna and coupler: top view.

Figure 17. (**a**) Diagram of the proposed antenna model of the chip. (**b**) The process model used.
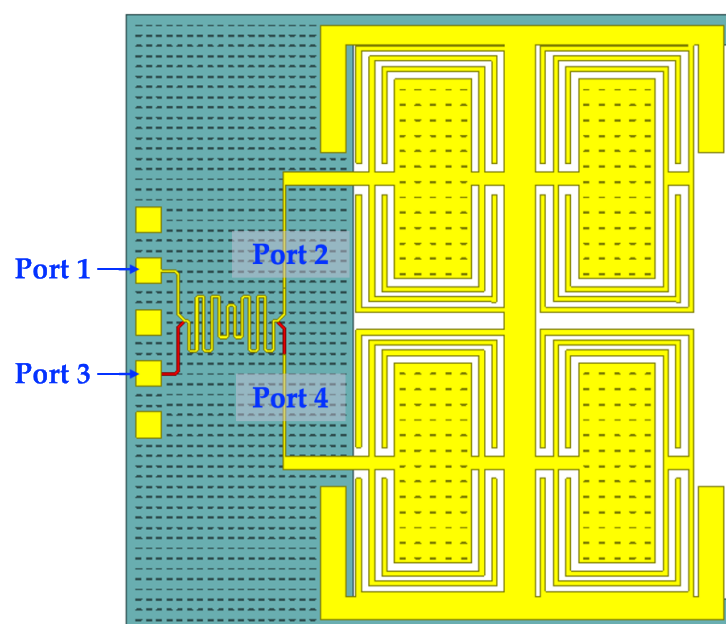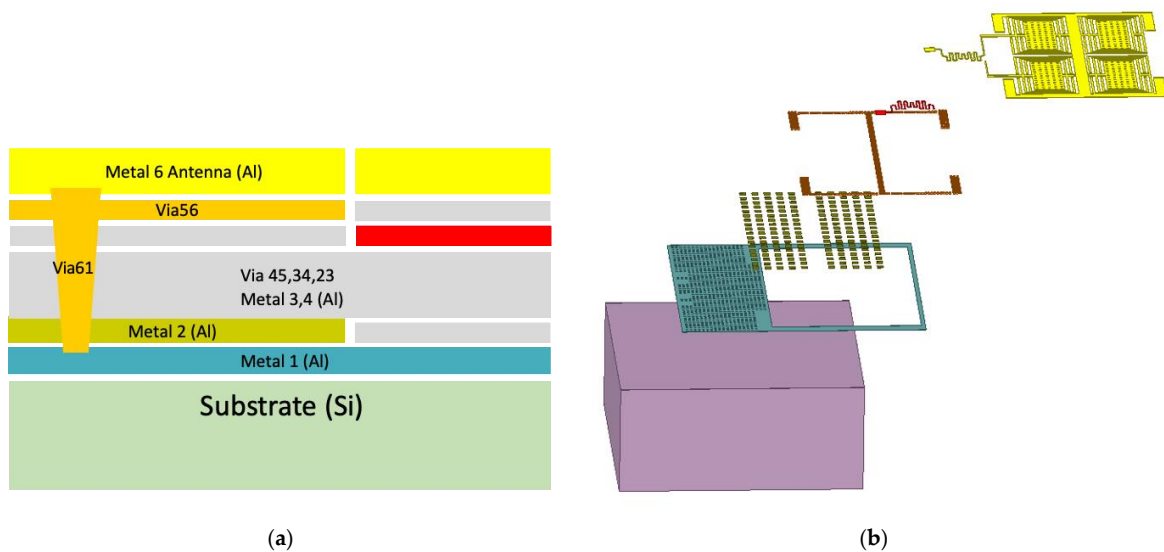
Figure 17b shows the structure of each metal layer stacked in an exploded view, which contributes to the miniaturization of the antenna area, unlike conventional microwave designs [1,72–74]. For antenna measurements, two inputs, port 1 and port 3, are excited with probes. No additional circuitry is required for the ground. Finally, in order to provide more freedom in optimizing the antenna characteristics, a trade-off was made in the overall antenna size, and a metal frame was used to wrap the antenna.

The distance between antennas is calculated as a multiple of $\lambda/4$ of 28 GHz. Equation (8) shows that E is the electrical length, L is the physical length, and c is the speed of light [75]. By calculation, the electrical length from port 1 of the parallel coupler input to port 2 of the antenna feed is 1335 µm, which is calculated using the application frequency band in this paper.

$$E = \frac{Lf\sqrt{\varepsilon_{eff}}}{c} \tag{8}$$

The port 1 to port 2 analog phase angle is -90 degrees, the port 1 to port 4 phase is -180 degrees, and the phase difference is -90 degrees, forming two parallel stacked couplers. In the signal conversion process, the input port 1 and port 2 will pass through the upper and lower bending parallel couplers, respectively. The simulation result of Figure 18 shows that after combining the coupler with the antenna, the standard $S_{11} < -10$ dB produces a bandwidth of 12~60 GHz. The port isolation is -6.5 dB.

Figure 19a–d shows the simulated 3D and 2D planar field patterns of the coupler antenna resonant frequency at 28 GHz, and it can be seen that the proposed coupler can actually achieve the beam control effect. The Eθ beam angles of $+45°$ and $+135°$ can be seen in the *x-z* plane for each of the port 1 and port 3 feeds of Figure 16, with an angular difference of $90°$. From the *x-z* plane field pattern section of Figure 19a,b, it can be observed that port 1 feeds in with a beam direction of $+135°$. The *x-z* plane field pattern section in Figure 19c,d shows that port 3 feeds in with a beam direction of $+45°$. When the coupler antenna feeds into the excitation of port 1 and port 3, it produces different phase radiation directions with an angular difference of $90°$ between them.
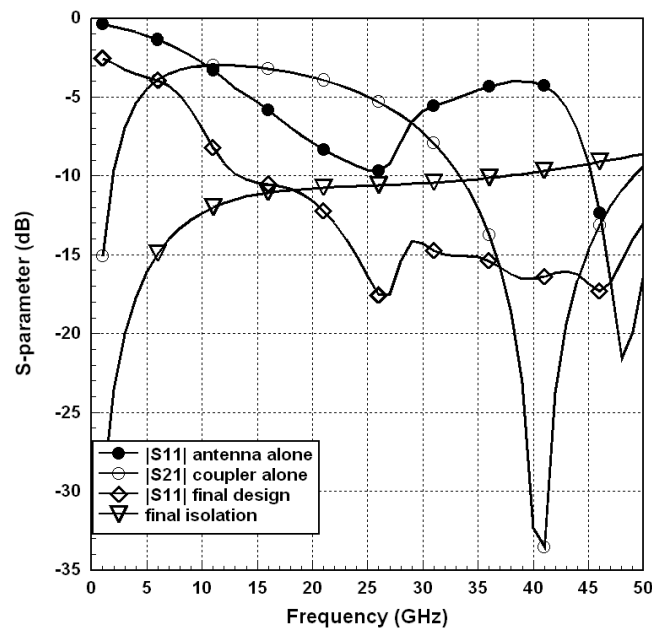
Figure 18. S parameters for coupler alone, antenna alone, and final design. The isolation of port 1 and port 3.
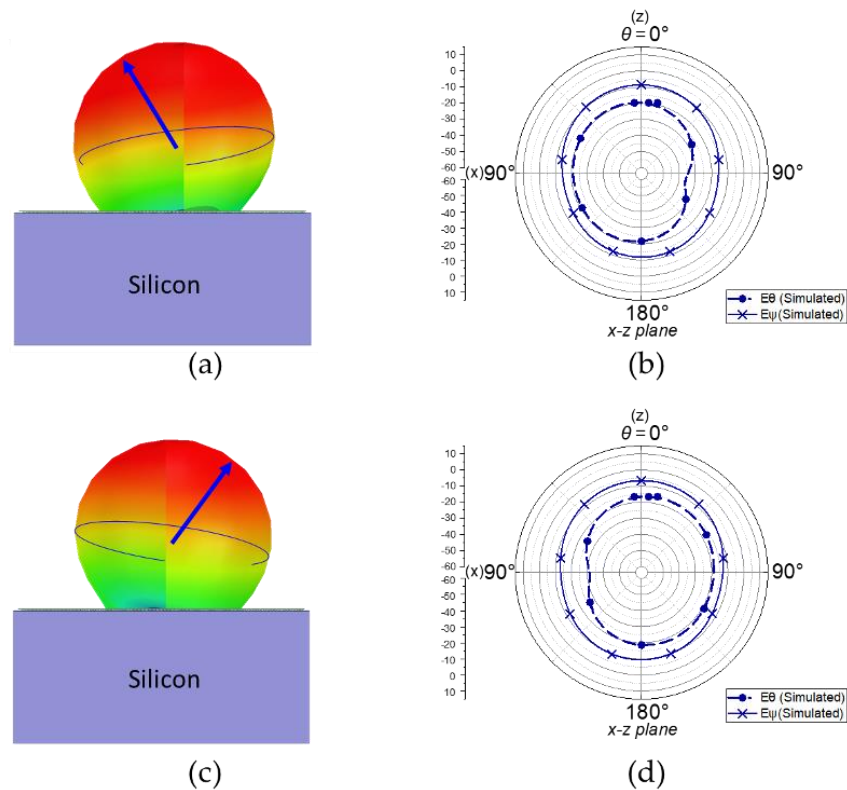
Figure 19. (**a**) 3D field pattern at port 1 feed, (**b**) *x-z* plane field pattern at port 1 feed, (**c**) 3D field pattern at port 3 feed, and (**d**) *x-z* plane field pattern at port 3 feed.

4. Power Density Simulation

The design takes into consideration the development of wearable devices, and the design of the microstrip patch antenna utilizes a different structure to generate radiation from the antenna. The power density is calculated by reflecting back to the antenna surface from the ground, which generates most of the radiation, and only a small portion of the radiation power is lost through the ground. When the antenna is operated in a human

environment, the human body absorbs the radiated energy from the lost electromagnetic waves. The long-term exposure or short-term absorption of high radiation levels can have negative health effects. To ensure public safety, the Federal Communications Commission (FCC) established the electromagnetic field (EMF) standard in 1996, and the FCC limits the public exposure specific absorption rate (SAR) of mobile devices to 1.6 W/kg. In high frequency states, the wavelength is very short, so the SAR is ignored in favor of power density. However, the wavelength is very short at a high frequency, so the SAR is ignored and the power density (PD) is calculated instead [58]. At frequencies above 10 GHz, EM waves may be absorbed by the human surface, resulting in an increase in temperature. This problem can be investigated by PD simulations, and Table 1 shows the specifications of the Federal Communications Commission (FCC), ICNIRP, and IEEE for PD values [76].

Table 1. Limit of power density.

	FCC	ICNIRP	IEEE	
Transition frequency (GHz)	6–100	10–300	3–30	30–100
Power density limit (W/m^2)	10	10	10	10

The PD safety limit is 10 W/m^2. The equation is as follows [77].

$$S_{inc}^m(A, d, \beta_\chi) = \frac{1}{A} \int_A |\text{Re}[E(d, \beta_\chi) \times H^*(d, \beta_\chi)]| d_s x \tag{9}$$

Figure 20 shows the input power of the antenna feed point at 0.1 W (20 dBm) and a frequency of 28 GHz to calculate the PD value.

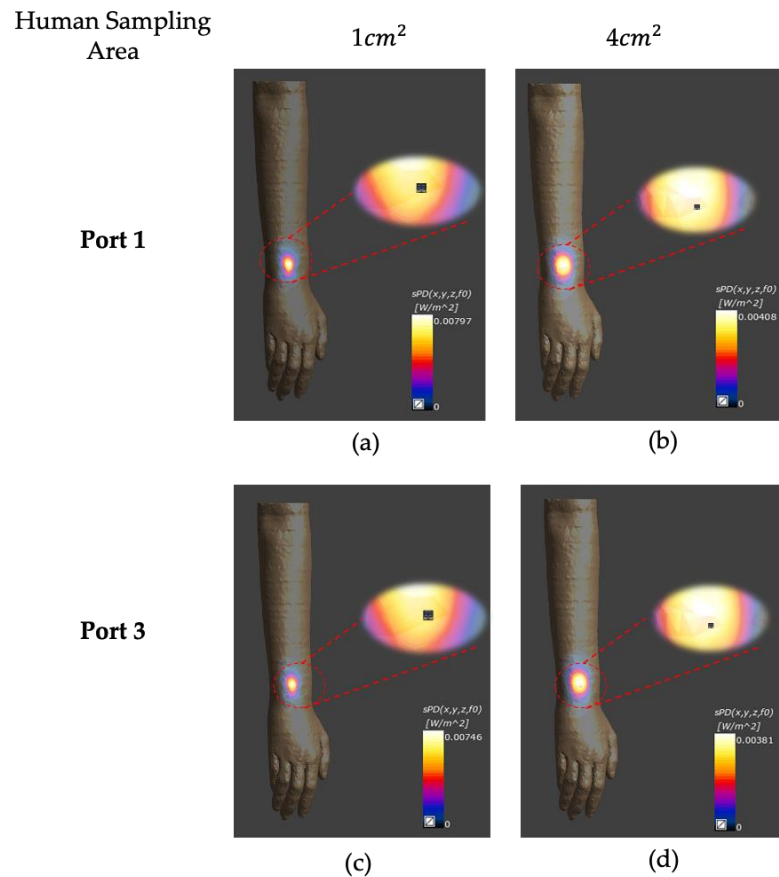**Figure 20.** Power density simulation. (**a**) Port 1 feed-in with a sample area of 1 cm^2, (**b**) port 1 feed-in with a sample area of 4 cm^2, (**c**) port 3 feed-in with a sample area of 1 cm^2, and (**d**) port 3 feed-in with a sample area of 4 cm^2.

When wearable devices support frequency bands above 6 GHz, power density (PD) measurements are required by FCC regulatory testing requirements. This paper uses Sim4Life to perform PD simulations. Figure 21 shows the power density simulation results when the signal is fed to the chip antenna. The input power from the feed point is 0.1 W (20 dBm) when the antenna is 10 mm away from the arm. Figure 20a,b shows the PD results of 1 cm^2 and 4 cm^2 sampling area when the wafer is fed from port 1. The PD results are shown in Figure 20c,d for the sampling area of 1 cm^2 and 4 cm^2 when the chip is fed from port 3. Simulation results show that the chip antenna has a maximum PD of 0.00797 W/m^2 at 28 GHz for a human sampling area of 1 cm^2 and 0.00381 W/m^2 at 4 cm^2, which is well below the certification limit of 10 W/m^2.

(**a**)   (**b**)

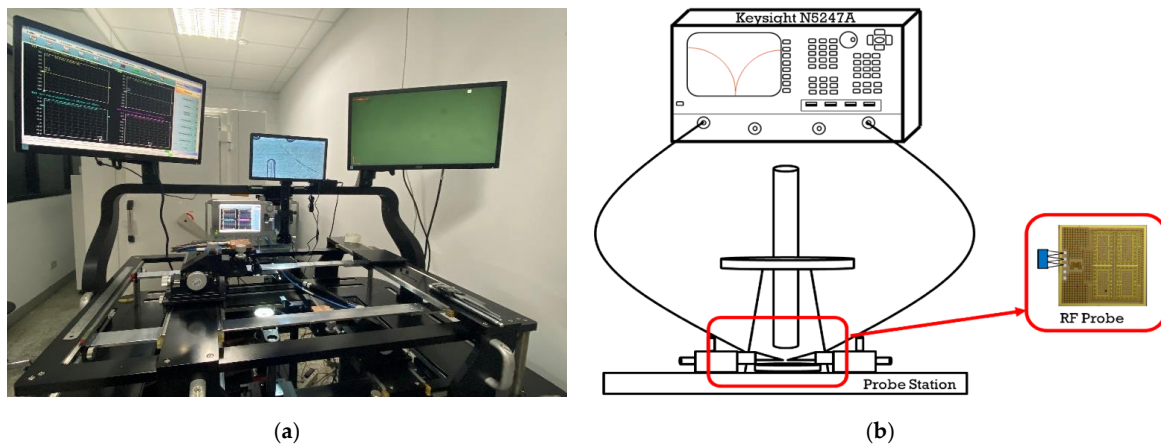**Figure 21.** (**a**) Measurement system. (**b**) Measurement schematic.

5. Experimental Setup and Results

5.1. Measurement System

The measurement system used in this study is shown in Figure 21a. The network analyzer used is Keysight N5247A PNA X Network Analyze, and the probe station is FAST AND BEST CO. The measurement range is from 10 MHz to 67 GHz, and Figure 21b shows the measurement schematic.

5.2. Measurement Results

The physical chip antenna is shown in Figure 22, and the size is 1.2 mm × 1.2 mm. When port 1 is excited, the antenna radiates a linearly polarized wave in the broadside direction. If port 3 is excited, the same phenomenon will occur as for port 1. Because the design of this paper is symmetric, the antennas operating at both ports should have very similar return losses. Therefore, in this article, only the far-field measurements using Port 1 excitation are shown.

Figure 23 shows the simulated and measured S-parameters. At −10 dB, the antenna measured an |S11| operating bandwidth of 115% (16.7–61.9 GHz). At −15 dB, the |S11| operating bandwidth is 84.7% (21.3–52.6 GHz). At −20 dB, it is 17.8% (23.55–28.11 GHz) and 14.71% (42.86–49.64 GHz), respectively. The antenna will be highly efficient since it is designed without the use of active components such as diodes or transistors, and the actual S11 measurements compare favorably with the simulated results.
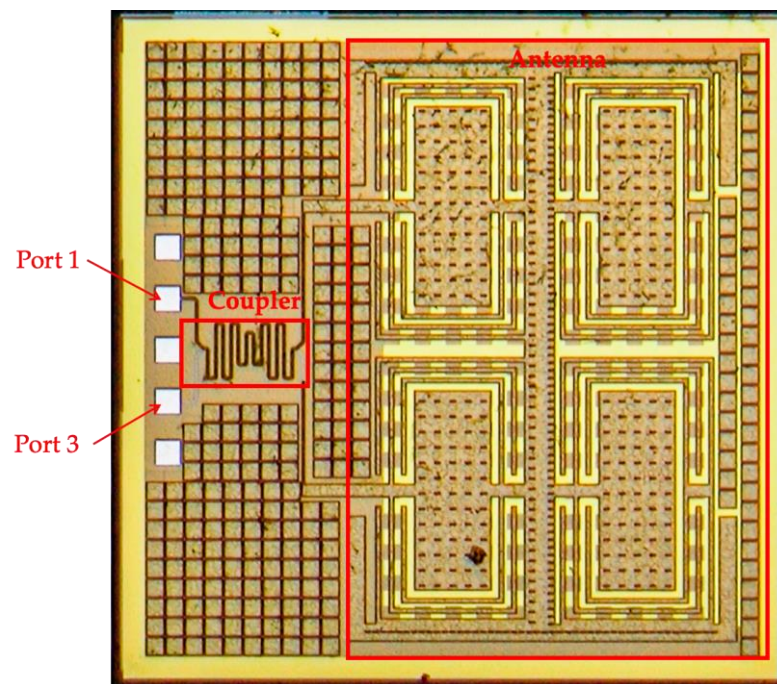
Figure 22. The actual chip. The chip size is 1.2 mm × 1.2 mm.
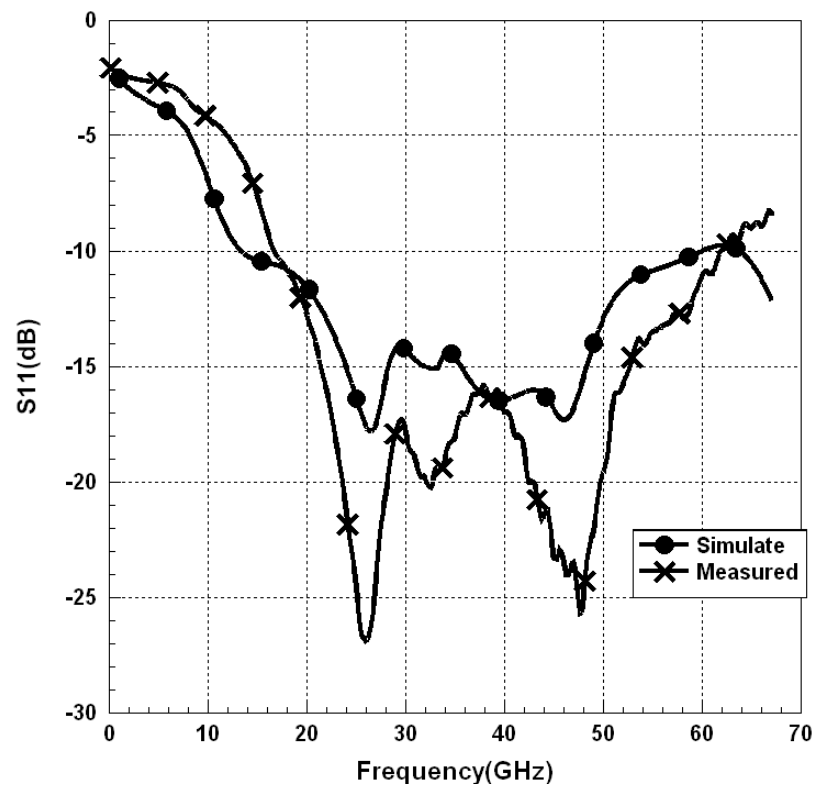
Figure 23. The proposed chip measurement results are compared with the simulated results.

Figure 24 shows the proposed antennas fed from port 1 and port 3, respectively. Observe the surface current distribution at 24 GHz, 28 GHz, and 32 GHz frequency points. When the frequency points are at 24 GHz and 32 GHz, the surface current distribution is not uniform and the surface current strength is weak, so the correct beam angle cannot be generated. In 28 GHz, the metal ring structure near the feedthrough has a stronger

symmetrical resonant current compared to 24 GHz and 32 GHz, which produces the correct beam angle.

Figure 24. The proposed antennas are fed into port 1 and port 3 to observe the surface current distribution at the 24 GHz, 28 GHz, and 32 GHz frequency points.

Table 2 shows the performance of the proposed coupler antenna compared to other coupler antennas of different architectures in the 28–30 GHZ band. The comparison includes the available bandwidth, size, and dimensions. It is clear that the proposed coupler antenna has a significant size advantage compared to other 28 GHz antennas.

Table 2. Comparison with other antennas.

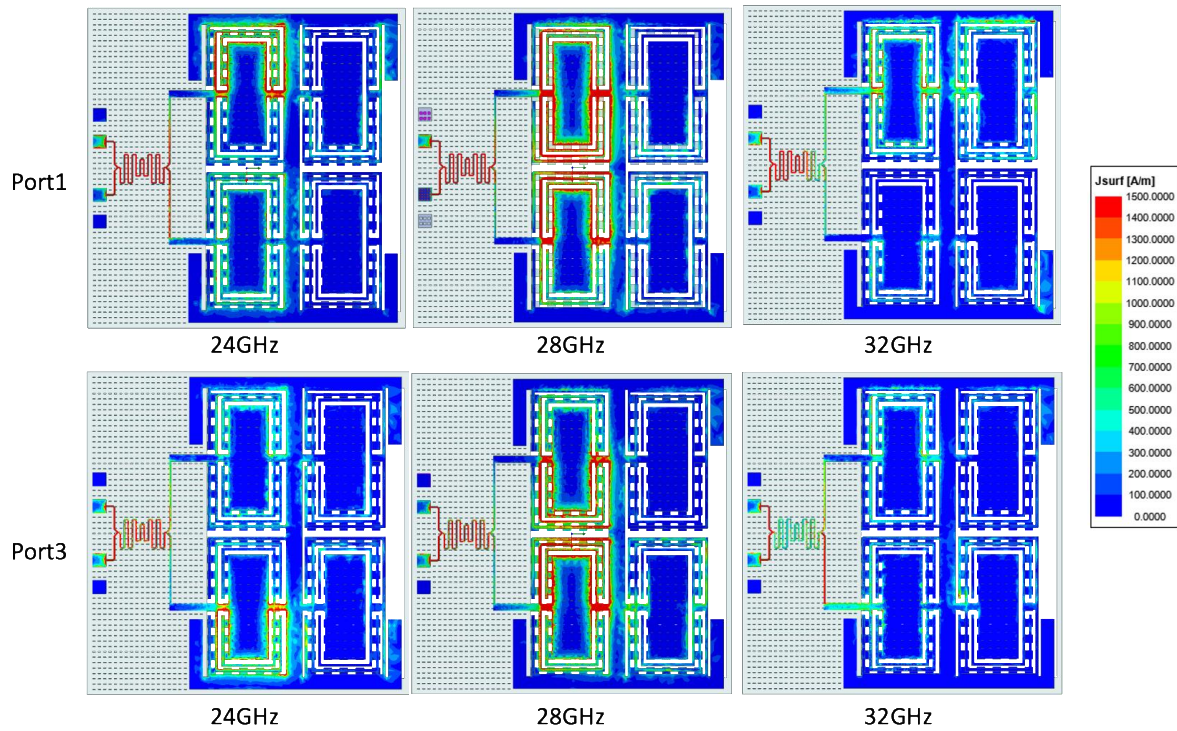|	Substrate	Coupler Type	Antenna Type	Center Frequency (GHz)	BW (%)	Return Loss (dB)	Phase Error (deg)	Overall Size
Proposed	180 μm CMOS	Parallel line coupler	Patch antenna	28	84.7	15	0.04	1.2 mm × 1.2 mm $0.216\lambda_0 \times 0.147\lambda_0$
[73]	PCB	Rat-race coupler	Differential Feeding antenna	30	27.90	15	±4	5.1 mm $0.51\lambda_0$
[74]	45 nm CMOS	Hybrid coupler	Array antenna	28	14.28	15	-	4 mm × 2.6 mm $0.746\lambda_0 \times 0.485\lambda_0$
[78]	PCB	Directional coupler	Millimeter-wave Multibeam array antenna	30	13.3	-	-	19.14 mm × 74.83 mm $2.84\lambda_0 \times 11.1\lambda_0$
[79]	120 nm SiGe	Hybrid coupler	Antenna array	28	24	-	2.3	4 mm × 3.8 mm $0.59\lambda_0 \times 0.56\lambda_0$

6. Conclusions

In conventional beam control designs, an extremely large structure is often used. This paper introduces a beam-switching chip patch antenna sensor with a wide available frequency band and excellent isolation characteristics. First the chip is designed as a square patch antenna in the form of a microstrip line, which is excited in a parallel manner by a

parallel coupler. By using the coupler, the desired beam direction can be adjusted by feeding the appropriate input endpoints. Finally, the results are verified by a real experiment and show a good agreement between measurement and simulation. It has a wide operating band of 84.7% (21.3–52.6 GHz) at S-parameter standards below −15 dB. Within this band, an isolation of more than 15 dB is achieved. In this design, the cost can be significantly reduced, the space used can be decreased, and the same effect can be achieved. Finally, the simulation was performed for power density. The simulated results show that it not only passes the FCC, ICNIRP, and IEEE standards but also is much lower than the standard and has very low damage to the human body, which is very suitable for wearable devices. Therefore, an antenna sensor can be applied to the surface of the human body for body measurement in the future, such as Blood Glucose Monitoring.

Author Contributions: Conceptualization, M.-A.C.; methodology, M.-A.C.; software, M.-A.C. and W.-J.L.; validation, M.-A.C., W.-J.L. and C.-W.L.; formal analysis, M.-A.C., W.-J.L. and C.-W.L.; investigation, C.-W.L., and W.-J.L.; resources, M.-A.C.; writing-original draft preparation, M.-A.C. and C.-W.L.; writing-review and editing, M.-A.C.; visualization, M.-A.C.; supervision, M.-A.C.; project administration, M.-A.C.; funding acquisition, M.-A.C. All authors have read and agreed to the published version of the manuscript.

Institutional Review Board Statement: Not applicable.

Informed Consent Statement: Not applicable.

Data Availability Statement: All data are included within manuscript.

References

1. Paquit, M.; Arapan, L.; Feng, W.; Friedt, J.-M. Long range passive RADAR interrogation of subsurface acoustic passive wireless sensors using terrestrial television signals. *IEEE Sens. J.* **2020**, *20*, 7156–7160. [CrossRef]
2. Hallil, H.; Dejous, C.; Hage-Ali, S.; Elmazria, O.; Rossignol, J.; Stuerga, D.; Talbi, A.; Mazzamurro, A.; Joubert, P.-Y.; Lefeuvre, E. Passive resonant sensors: Trends and future prospects. *IEEE Sens. J.* **2021**, *21*, 12618–12632. [CrossRef]
3. Gomez-del-Hoyo, P.; del-Rey-Maestre, N.; Jarabo-Amores, M.-P.; Mata-Moya, D.; Benito-Ortiz, M.-d.-C. Improved 2D Ground Target Tracking in GPS-Based Passive Radar Scenarios. *Sensors* **2022**, *22*, 1724. [CrossRef]
4. Speirs, P.J.; Ummenhofer, M.; Schüpbach, C.; Renker, M.; Wellig, P.; Cristallini, D.; O'Hagan, D.W.; Kohler, M.; Murk, A. Comparison of DVB-T Passive Radar Simulated and Measured Bistatic RCS Values for a Pilatus PC-12 Aircraft. *Sensors* **2022**, *22*, 2766. [CrossRef]
5. Knioła, M.; Rogala, T.; Szczepaniak, Z. Counter-Passive Coherent Locator (C-PCL)—A Method of Remote Detection of Passive Radars for Electronic Warfare Systems. *Electronics* **2021**, *10*, 1625. [CrossRef]
6. Prasanna, R.; Annaram, K.; Shanker, N. Multilayer Flexible Substrate Antenna Sensor for PT Measurement From Blood Plasma to Avoid Turbidity and Reagent Sensitivity Variations Through Regression Modelling. *IEEE Sens. J.* **2021**, *21*, 10409–10419. [CrossRef]
7. Tajin, M.A.S.; Mongan, W.M.; Dandekar, K.R. Passive RFID-based diaper moisture sensor. *IEEE Sens. J.* **2020**, *21*, 1665–1674. [CrossRef]
8. Rivera-Lavado, A.; García-Lampérez, A.; Jara-Galán, M.-E.; Gallo-Valverde, E.; Sanz, P.; Segovia-Vargas, D. Low-Cost Electromagnetic Split-Ring Resonator Sensor System for the Petroleum Industry. *Sensors* **2022**, *22*, 3345. [CrossRef]
9. Dash, L.; Pattanayak, B.K.; Mishra, S.K.; Sahoo, K.S.; Jhanjhi, N.Z.; Baz, M.; Masud, M. A Data Aggregation Approach Exploiting Spatial and Temporal Correlation among Sensor Data in Wireless Sensor Networks. *Electronics* **2022**, *11*, 989. [CrossRef]
10. Yu, Z.; Fu, Y. A Passive Location Method Based on Virtual Time Reversal of Cross Antenna Sensor Array and Tikhonov Regularized TLS. *IEEE Sens. J.* **2021**, *21*, 21931–21940. [CrossRef]
11. Storrer, L.; Yildirim, H.C.; Crauwels, M.; Copa, E.I.P.; Pollin, S.; Louveaux, J.; De Doncker, P.; Horlin, F. Indoor tracking of multiple individuals with an 802.11 ax Wi-Fi-based multi-antenna passive radar. *IEEE Sens. J.* **2021**, *21*, 20462–20474. [CrossRef]
12. Al-Jarrah, M.A.; Al-Dweik, A.; Ali, N.T.; Alsusa, E. Joint estimation of location and orientation in wireless sensor networks using directional antennas. *IEEE Sens. J.* **2020**, *20*, 14347–14359. [CrossRef]
13. Suchodolski, T. Active Control Loop of the BOROWIEC SLR Space Debris Tracking System. *Sensors* **2022**, *22*, 2231. [CrossRef]
14. Jouali, R.; Aoutoul, M.; Ouahmane, H.; Ahmad, S.; Had, A.; El Moukhtafi, F.; Parchin, N.O.; See, C.H.; Abd-Alhameed, R. Design of an Analog RFID-Based Tag Antenna with Opened Circuited L-Shaped Stubs for Applications in Localization. *Electronics* **2022**, *11*, 1027. [CrossRef]

15. Tao, Y.; Wu, L.; Sidén, J.; Wang, G. Monte Carlo-Based Indoor RFID Positioning with Dual-Antenna Joint Rectification. *Electronics* **2021**, *10*, 1548. [CrossRef]
16. Yao, Y.; Ge, Q.; Yu, J.; Chen, X. A Novel Antenna for UHF RFID Near-Field Applications. *Electronics* **2021**, *10*, 1310. [CrossRef]
17. Behera, S.K. Chipless RFID Sensors for Wearable Applications: A Review. *IEEE Sens. J.* **2021**, *22*, 1105–1120. [CrossRef]
18. Zhu, W.; Zhang, Q.; Matlin, M.; Chen, Y.; Wu, Y.; Zhu, X.; Zhao, H.; Pollack, R.; Xiao, H. Passive digital sensing method and its implementation on passive RFID temperature sensors. *IEEE Sens. J.* **2020**, *21*, 4793–4800. [CrossRef]
19. Benouakta, S.; Hutu, F.D.; Duroc, Y. UHF RFID Temperature Sensor Tag Integrated into a Textile Yarn. *Sensors* **2022**, *22*, 818. [CrossRef]
20. Kumar, V.; Kumar, R.; Khan, A.A.; Kumar, V.; Chen, Y.-C.; Chang, C.-C. RAFI: Robust Authentication Framework for IoT-Based RFID Infrastructure. *Sensors* **2022**, *22*, 3110. [CrossRef]
21. Savill, T.; Jewell, E. Design of a Chipless RFID Tag to Monitor the Performance of Organic Coatings on Architectural Cladding. *Sensors* **2022**, *22*, 3312. [CrossRef]
22. Mohammadi, P.; Mohammadi, A.; Demir, S.; Kara, A. Compact size, and highly sensitive, microwave sensor for non-invasive measurement of blood glucose level. *IEEE Sens. J.* **2021**, *21*, 16033–16042. [CrossRef]
23. Sabban, A. Wearable Circular Polarized Antennas for Health Care, 5G, Energy Harvesting, and IoT Systems. *Electronics* **2022**, *11*, 427. [CrossRef]
24. Subahi, A.F.; Bouazza, K.E. An intelligent IoT-based system design for controlling and monitoring greenhouse temperature. *IEEE Access* **2020**, *8*, 125488–125500. [CrossRef]
25. Kong, X.; Xu, Y.; Jiao, Z.; Dong, D.; Yuan, X.; Li, S. Fault location technology for power system based on information about the power internet of things. *IEEE Trans. Ind. Inform.* **2019**, *16*, 6682–6692. [CrossRef]
26. Bedi, G.; Venayagamoorthy, G.K.; Singh, R.; Brooks, R.R.; Wang, K.-C. Review of Internet of Things (IoT) in electric power and energy systems. *IEEE Internet Things J.* **2018**, *5*, 847–870. [CrossRef]
27. Omer, A.E.; Safavi-Naeini, S.; Hughson, R.; Shaker, G. Blood Glucose Level Monitoring Using an FMCW Millimeter-Wave Radar Sensor. *Remote Sens.* **2020**, *12*, 385. [CrossRef]
28. Roshani, S.; Yahya, S.I.; Roshani, S.; Farahmand, A.H.; Hemmati, S. Design of a Modified Compact Coupler with Unwanted Harmonics Suppression for L-Band Applications. *Electronics* **2022**, *11*, 1747. [CrossRef]
29. Ghaffarian, M.S.; Moradi, G.; Khajehpour, S.; Honari, M.M.; Mirzavand, R. Dual-Band/Dual-Mode Rat-Race/Branch-Line Coupler Using Split Ring Resonators. *Electronics* **2021**, *10*, 1812. [CrossRef]
30. Zaman, M.S.; Morshed, B.I. A low-power portable scanner for body-worn Wireless Resistive Analog Passive (WRAP) sensors for mHealth applications. *Measurement* **2021**, *177*, 109214. [CrossRef]
31. Liu, Z.; Yu, H.; Zhou, K.; Li, R.; Guo, Q. Influence of Volumetric Damage Parameters on Patch Antenna Sensor-Based Damage Detection of Metallic Structure. *Sensors* **2019**, *19*, 3232. [CrossRef]
32. Liu, Z.; Guo, Q.; Wang, Y.; Lu, B. Decoupled Monitoring Method for Strain and Cracks Based on Multilayer Patch Antenna Sensor. *Sensors* **2021**, *21*, 2766. [CrossRef]
33. Julrat, S.; Trabelsi, S. Measuring dielectric properties for sensing foreign material in peanuts. *IEEE Sens. J.* **2018**, *19*, 1756–1766. [CrossRef]
34. Balanis, C.A. *Antenna Theory: Analysis and Design*; John Wiley & Sons: Hoboken, NJ, USA, 2015.
35. Hu, J.; Li, Y.; Zhang, Z. A Novel Reconfigurable Miniaturized Phase Shifter for 2-D Beam Steering 2-Bit Array Applications. *IEEE Microw. Wirel. Compon. Lett.* **2021**, *31*, 381–384. [CrossRef]
36. Xin, Z.; Donglin, S. Digital processing system for digital beam forming antenna. In Proceedings of the 2005 IEEE International Symposium on Microwave, Antenna, Propagation and EMC Technologies for Wireless Communications, Beijing, China, 8–12 August 2005; IEEE: Beijing, China, 2005; pp. 173–175.
37. Xiong, Y.; Zeng, X.; Li, J. A tunable concurrent dual-band phase shifter MMIC for beam steering applications. *IEEE Trans. Circuits Syst. II Express Briefs* **2020**, *67*, 2412–2416. [CrossRef]
38. Kim, S.; Yoon, S.; Lee, Y.; Shin, H. A Miniaturized Butler Matrix Based Switched Beamforming Antenna System in a Two-Layer Hybrid Stackup Substrate for 5G Applications. *Electronics* **2019**, *8*, 1232. [CrossRef]
39. Zhao, X.; Shah, U.; Glubokov, O.; Oberhammer, J. Micromachined subterahertz waveguide-integrated phase shifter utilizing supermode propagation. *IEEE Trans. Microw. Theory Tech.* **2021**, *69*, 3219–3227. [CrossRef]
40. Ali, Q.; Shahzad, W.; Ahmad, I.; Safiq, S.; Bin, X.; Abbas, S.M.; Sun, H. Recent Developments and Challenges on Beam Steering Characteristics of Reconfigurable Transmitarray Antennas. *Electronics* **2022**, *11*, 587. [CrossRef]
41. Lin, Y.-H.; Tsai, Z.-M. Frequency-reconfigurable phase shifter based on a 65-nm CMOS process for 5G applications. *IEEE Trans. Circuits Syst. II Express Briefs* **2021**, *68*, 2825–2829. [CrossRef]
42. Londhe, S.; Socher, E. 28–38-GHz 6-bit Compact Passive Phase Shifter in 130-nm CMOS. *IEEE Microw. Wirel. Compon. Lett.* **2021**, *31*, 1311–1314. [CrossRef]
43. Lee, I.-G.; Kim, J.-Y.; Hong, I.-P. Design of Multi-Functional Transmitarray with Active Linear Polarization Conversion and Beam Steering Capabilities. *Appl. Sci.* **2022**, *12*, 4319. [CrossRef]
44. Sánchez-Escuderos, D.; Herranz-Herruzo, J.I.; Ferrando-Rocher, M.; Valero-Nogueira, A. True-time-delay mechanical phase shifter in gap waveguide technology for slotted waveguide arrays in Ka-band. *IEEE Trans. Antennas Propag.* **2020**, *69*, 2727–2740. [CrossRef]

45. Górniak, P. Modeling of the 5G-Band Patch Antennas Using ANNs under the Uncertainty of the Geometrical Design Parameters Associated with the Manufacturing Process. *Algorithms* **2022**, *15*, 7. [CrossRef]

46. Luo, Y.; Gu, Y.; Zhang, H.; Xu, J.; Qian, F.; Yang, G.; Cui, H. A Wideband mmWave Microstrip Patch Antenna Based on Zero-Mode and TM-Mode Resonances. *Electronics* **2022**, *11*, 1234. [CrossRef]

47. Pauli, M.; Göttel, B.; Scherr, S.; Bhutani, A.; Ayhan, S.; Winkler, W.; Zwick, T. Miniaturized millimeter-wave radar sensor for high-accuracy applications. *IEEE Trans. Microw. Theory Tech.* **2017**, *65*, 1707–1715. [CrossRef]

48. Chen, D.; Vakalis, S.; Nanzer, J.A. Imageless shape detection using a millimeter-wave dynamic antenna array and noise illumination. *IEEE Trans. Microw. Theory Tech.* **2021**, *70*, 758–765. [CrossRef]

49. Kim, S. Inkjet-Printed Electronics on Paper for RF Identification (RFID) and Sensing. *Electronics* **2020**, *9*, 1636. [CrossRef]

50. Nie, H.-K.; Xuan, X.-W.; Shi, Q.; Guo, A.; Li, M.-J.; Li, H.-J.; Ren, G.-J. Wearable Antenna Sensor Based on EBG Structure for Cervical Curvature Monitoring. *IEEE Sens. J.* **2021**, *22*, 315–323. [CrossRef]

51. Agwil, R.O.; Benchikh, S.; Djillali, H.; Tatu, S.O. Antenna rectifier using quadrature hybrid coupler for power-harvesting applications. *Int. J. RF Microw. Comput.-Aided Eng.* **2020**, *30*, e22279. [CrossRef]

52. Maleki, A.; Oskouei, H.D.; Mohammadi Shirkolaei, M. Miniaturized microstrip patch antenna with high inter-port isolation for full duplex communication system. *Int. J. RF Microw. Comput.-Aided Eng.* **2021**, *31*, e22760. [CrossRef]

53. Sedra, A.S.; Smith, K.C.; Carusone, T.C.; Gaudet, V. *Microelectronic Circuits*; Oxford University Press: New York, NY, USA, 2004; Volume 4.

54. Lammert, V.; Hamouda, M.; Weigel, R.; Issakov, V. A 122 GHz On-Chip 3-Element Patch Antenna Array with 10 GHz Bandwidth. In Proceedings of the 2020 50th European Microwave Conference (EuMC), Utrecht, The Netherlands, 12–14 January 2021; IEEE: Utrecht, The Netherlands, 2021; pp. 599–602.

55. Zhang, Z.; Cheng, Z.; Ke, H.; Liu, G. A broadband high-efficiency power amplifier by using branch line coupler. *IEEE Microw. Wirel. Compon. Lett.* **2020**, *30*, 880–883. [CrossRef]

56. Zhu, X.; Yang, T.; Chi, P.-L.; Xu, R. Novel reconfigurable filtering rat-race coupler, branch-line coupler, and multiorder bandpass filter with frequency, bandwidth, and power division ratio control. *IEEE Trans. Microw. Theory Tech.* **2020**, *68*, 1496–1509. [CrossRef]

57. Lai, J.; Yang, T.; Chi, P.-L.; Xu, R. Novel Evanescent-Mode Cavity Filter With Reconfigurable Rat-Race Coupler, Quadrature Coupler and Multi-Pole Filtering Functions. *IEEE Access* **2020**, *8*, 32688–32697. [CrossRef]

58. Feng, W.; Duan, X.; Shi, Y.; Zhou, X.Y.; Che, W. Dual-band branch-line couplers with short/open-ended stubs. *IEEE Trans. Circuits Syst. II Express Briefs* **2020**, *67*, 2497–2501. [CrossRef]

59. Deng, P.-H.; Li, M.-W.; Chen, W.-T.; Lin, C.-H.; Lu, C.-H.; Tsai, R.-F.; Chen, K.-H. Designs of Branch-Line Couplers by Considering the Parasitic Effects of PIN Diodes. *IEEE Access* **2020**, *8*, 223089–223100. [CrossRef]

60. Tan, X.; Sun, J.; Lin, F. A compact frequency-reconfigurable rat-race coupler. *IEEE Microw. Wirel. Compon. Lett.* **2020**, *30*, 665–668. [CrossRef]

61. Zaidi, A.M.; Beg, M.Z.; Kanaujia, B.K.; Rawat, K.; Kumar, S. Rambabu, K.; Singh, S.P.; Lay-Ekuakille, A. A Dual-Band Rat-Race Coupler for High Band Ratio Wireless Applications. *IEEE Trans. Instrum. Meas.* **2021**, *70*, 2006806. [CrossRef]

62. Zheng, Y.; Wang, W.; Yang, Y.; Wu, Y. Single-layer planar wideband rat-race coupler using a shorted parallel-coupled multi-line section. *IEEE Trans. Circuits Syst. II Express Briefs* **2020**, *67*, 3053–3057. [CrossRef]

63. Tseng, S.-Y. Robust Light Coupling in a Quadratically Bent Directional Coupler. *IEEE Photonics Technol. Lett.* **2021**, *33*, 343–346. [CrossRef]

64. Thirupathaiah, K.; Rao, L.K.; Ravi, B. Nanoplasmonic Directional Coupler Using Asymmetric Parallel Coupled MIM Waveguides. *IEEE Photonics Technol. Lett.* **2022**, *34*, 401–404. [CrossRef]

65. Sutbas, B.; Ozbay, E.; Atalar, A. Accurate isolation networks in quadrature couplers and power dividers. *IEEE Trans. Circuits Syst. II Express Briefs* **2020**, *68*, 1148–1152. [CrossRef]

66. Chen, Z.; Wu, Y.; Yang, Y.; Wang, W. A Novel Unequal Lumped-Element Coupler With Arbitrary Phase Differences and Arbitrary Impedance Matching. *IEEE Trans. Circuits Syst. II Express Briefs* **2021**, *69*, 369–373. [CrossRef]

67. Nasr, M.A.; Kishk, A.A. Analysis and design of broadband ridge-gap-waveguide tight and loose hybrid couplers. *IEEE Trans. Microw. Theory Tech.* **2020**, *68*, 3368–3378. [CrossRef]

68. Zhu, H.; Zhang, T.; Guo, Y.J. Wideband Hybrid Couplers With Unequal Power Division/Arbitrary Output Phases and Applications to Miniaturized Nolen Matrices. *IEEE Transactions on Microwave Theory and Techniques* **2022**, *70*, 3040–3053. [CrossRef]

69. Chin, T.-Y.; Chang, S.-F.; Chang, C.-C.; Wu, J.-C. A 24-GHz CMOS Butler Matrix MMIC for multi-beam smart antenna systems. In Proceedings of the 2008 IEEE Radio Frequency Integrated Circuits Symposium, Atlanta, GA, USA, 15-17 June 2008; IEEE: Atlanta, GA, USA, 2008; pp. 633–636.

70. Panda, R.A.; Dash, P.; Mandi, K.; Mishra, D. Gain enhancement of a biconvex patch antenna using metallic rings for 5G application. In Proceedings of the 2019 6th International Conference on Signal Processing and Integrated Networks (SPIN), Noida, India, 7–8 March 2019; IEEE: Noida, India, 2019; pp. 840–844.

71. Singh, H.; Mandal, S.K. Miniaturized on-chip meandered loop antenna with improved gain using partially shield layer. In Proceedings of the 2020 14th European Conference on Antennas and Propagation (EuCAP), Copenhagen, Denmark, 15–20 March 2020; IEEE: Copenhagen, Denmark, 2020; pp. 1–4.

72. Li, A.; Luk, K.-M. Millimeter-wave dual linearly polarized endfire antenna fed by 180° hybrid coupler. *IEEE Antennas Wirel. Propag. Lett.* **2019**, *18*, 1390–1394. [CrossRef]
73. Afifi, I.; Sebak, A.R. Wideband printed ridge gap rat-race coupler for differential feeding antenna. *IEEE Access* **2020**, *8*, 78228–78235. [CrossRef]
74. Singh, T.; Khaira, N.K.; Mansour, R.R. Thermally actuated SOI RF MEMS-based fully integrated passive reflective-type analog phase shifter for mmWave applications. *IEEE Trans. Microw. Theory Tech.* **2020**, *69*, 119–131. [CrossRef]
75. Pozar, D.M. *Microwave Engineering*; John Wiley & Sons: Hoboken, NJ, USA, 2011.
76. Islam, S.; Zada, M.; Yoo, H. Low-pass filter based integrated 5G smartphone antenna for sub-6-GHz and mm-wave bands. *IEEE Trans. Antennas Propag.* **2021**, *69*, 5424–5436. [CrossRef]
77. He, W.; Xu, B.; Yao, Y.; Colombi, D.; Ying, Z.; He, S. Implications of incident power density limits on power and EIRP levels of 5G millimeter-wave user equipment. *IEEE Access* **2020**, *8*, 148214–148225. [CrossRef]
78. Sun, Q.; Ban, Y.-L.; Lian, J.-W.; Liu, Y.; Nie, Z. Millimeter-wave multibeam antenna based on folded C-type SIW. *IEEE Trans. Antennas Propag.* **2020**, *68*, 3465–3476. [CrossRef]
79. Yeh, Y.-S.; Floyd, B.A. Multibeam phased-arrays using dual-vector distributed beamforming: Architecture overview and 28 GHz transceiver prototypes. *IEEE Trans. Circuits Syst. I Regul. Pap.* **2020**, *67*, 5496–5509. [CrossRef]